Proceedings of the ISSSRNS '92, Jaszowiec 1992

THE IMAGES OF DISLOCATIONS IN SYNCHROTRON BRAGG-CASE SECTION TOPOGRAPHY OF DIAMOND

W. WIERZCHOWSKI

Institute of Electronic Materials Technology, Wólczyńska 133, 01-919 Warsaw, Poland

AND M. MOORE

Department of Physics, Royal Holloway and Bedford New College
University of London, Egham, Surrey, TW20 0EX, UK

Bragg-case synchrotron section topographs were studied in parallel slabs cut from a synthetic diamond of a good quality. The topographs revealed the Pendellösung fringes and images of dislocations and other defects containing several fringe systems. The experiment provided the opportunity for studying of the theoretical dislocation images obtained by numerical integration of the Takagi–Taupin equations. A program employing a variable step of integration in the Bragg-case has been presented. The influence of the finite slit width and of the limited beam divergence on the theoretical images is also discussed.

PACS numbers: 61.10.–i, 61.70.–r

1. Introduction

The experiments with Bragg-case section topography were reported by a number of authors: Uragami [1] and Lang and Mai Zhen-Hong [2] firstly demonstrated the systems of Pendellösung fringes in perfect crystals, described theoretically by Uragami [1] and Afanasev and Kohn [3]. Zielińska-Rohozińska [4] presented experimental Bragg-case section images of dislocations. Bąk et al. [5] examined experimental and theoretical Pendellösung fringes in silicon samples bent by oxide layers.

In the present experiment we studied Bragg-case section topographs in a parallel slab prepared from a large synthetic diamond grown by the reconstitution method. Thanks to a very small absorption of X-rays in diamond the beam reflected from rear surface was visible in present topographs. Both the Pendellösung fringes and fringes due to the growth sector boundaries, stacking faults and dislocations were observed.

In the present paper the general character of experimental images of dislocations is compared with theoretical images obtained by numerical integration of the Takagi–Taupin equations. We used a numerical program adopting the idea of variable step algorithm, proposed previously by Petrashen [6] and widely used by Epelboin [7].

2. Experimental

The sample was prepared from the octahedral synthetic diamond by sawing and polishing surfaces perpendicular to the main [100] growth axis. The dimensions of the sample were $4 \times 4 \times 0.7$ mm^3 and it contained low density of dislocations in approximately two thirds of its volume.

Prior to the Bragg-case section experiments the sample was examined with other methods of X-ray topography and with cathodoluminescence topography. Some of these experiments are described in Ref. [8]. In particular, the Burgers vector and crystallographic type of more than 30 individual dislocations were determined from a set of Lang topographs in (111)- and (220)-type reflections from all equivalent crystallographic planes.

The Bragg-case section topographs were obtained at the station 7.6 in the S.E.R.C. Daresbury Laboratory. The camera was located at the distance of 80 m from the tangent point of the storage ring. It is easy to evaluate, taking the vertical dimension of the electron beam 0.4 mm, that the incident beam was collimated to 1 angular seconds (4 μrad).

We discuss here the topographs taken in symmetrical (400) reflection with the Bragg angle of 45°, selecting the radiation of 1.26 Å. The images were not absolutely free from higher harmonic but the contribution due to that is not very significant, in view of 10 times smaller intensity in the synchrotron spectrum and a much narrower reflection range.

The slit width of 12–15 μm was more than 1.5 times smaller than the extinction range for the (400) reflection, evaluated as 23 μm. Series of topographs were taken with the slit remotely translated and the beam intersecting different regions of the crystal.

Actually obtained topographs correspond to σ-polarized radiation thanks to almost complete polarization of the synchrotron radiation and the Bragg angle equal to 45°.

3. The method of numerical simulation

The principle of the variable step algorithm consists of the use of small integration steps close to the margin of the Borrmann triangle and in the region close to the dislocation core. In the other parts of the integration grid the steps of integration increase reducing the number of integration points and the time of computation.

The grid of integration for actual Bragg-case section topography is shown in Fig. 1. The increase or decrease of the step along s_h must be fitted on the surfaces of the crystal by increase or decrease of the step along the s_0 in the same

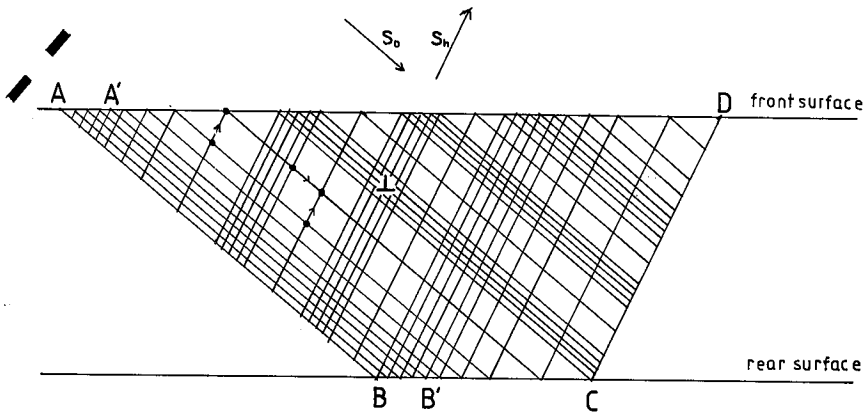

Fig. 1. Actually used integration grid for Bragg-case section topography in a slab of finite thickness adopting variable step algorithm. The additional number of small steps in AA′ enables taking into account the finite width of the slit.

ratio. An additional number of the smallest steps is introduced in the segment AA′ corresponding to the finite width of the slit.

We examined two different ways of taking into account the finite slit of the beam. The first one was realized by adding a number of sections with single points of excitation in AA′. It corresponds well to section experiments with conventional source of radiation, when the limitation of the beam divergence is relatively low.

The other method corresponds to the situation in the synchrotron experiments, when the long distance from the tangent point reduces the angular divergence to less than 1″. In this case we added at least 60 images with all points in AA′ excited, differing in the angle of incidence. The components correspond to a plane wave with wave front limited by a finite slit. In both cases the time consuming calculation of deformation field is performed only once for each plane of incidence and the stored values are used in calculation of other components.

We used the form of Takagi equations including the photoelectric absorption [9]. The amplitudes are obviously put equal to 0 in the points of the grid parallel to AB on the right side to the first excited point. In the segment BC on the rear surface we put the reflected beam amplitude equal to 0.

The anisotrophy of diamond is relatively low, as the parameter $A = 2c_{44}/(c_{11} - c_{12})$ is equal to 1.21 and the parameter $B = (\mu_V - \mu_R)/\mu_R$ is close to 0.15. Subscripts V and R denotes Voigt and Reuss averages of shear modulus, respectively. Hence according to Epelboin et al. [10] it was sufficiently accurate to use the isotropic approximation of the deformation field. This enabled us to take into account the relaxation of stress at the free surface. The deformation was calculated basing on the paper of Shaibani and Hazzledine [11].

The simulated topographs were printed with 36-dot module providing 37 tone grey scale. The simulations consist of 400 lines, obtained from 200 calculated planes of incidence. Each line contains 400 points obtained by averaging and extrapolation from a variable number of differently spaced points.

4. Results and discussion

A representative experimental Bragg-case synchrotron section topographs are shown in Fig. 2. The topographs exhibit interference Pendellösung fringes close to the incident beam. We can notice the trace of the incident beam reflected from the rear surface in the form of narrow strip sometimes followed by an area of enhanced intensity.

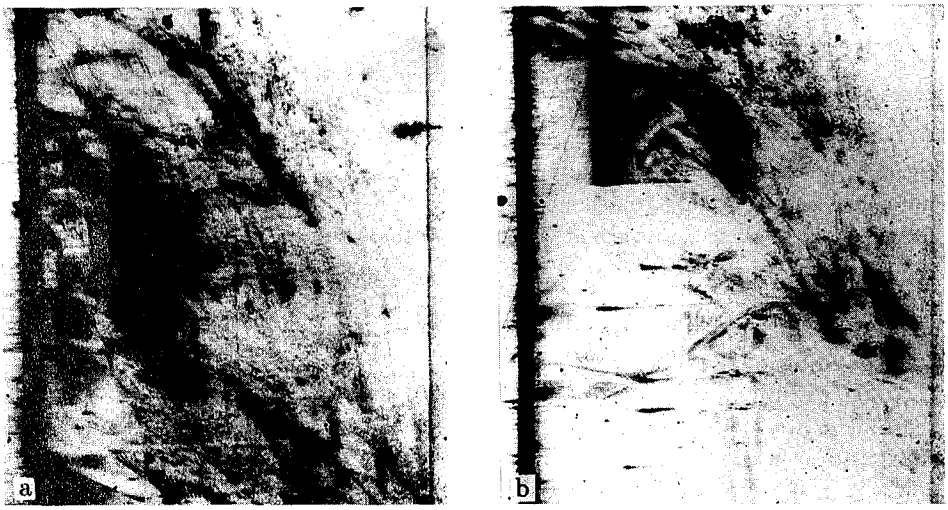

Fig. 2. Representative Bragg-case synchrotron section topographs in (400) symmetrical reflection of 1.26 Å radiation of $4 \times 4 \times 0.7$ mm^3 diamond slab. The diffraction vector is located horizontally. Some images of dislocations producing interference fringes are visible especially in the upper part of (a). The image of stacking fault also producing some fringes is visible in the upper part of (b).

The presented topographs contain images of stacking faults, grow sector boundaries and dislocations. It may be found in the topographs that all these defects can produce the interference fringes but the visibility of these fringes is dependent on the vicinity of a particular defect.

The most distinct and regular fringe patterns were observed in the case of stacking faults. Also the fringes due to some growth sector boundaries are usually distinct, but less regular. There were relatively many dislocations images in the section topographs but most of them were not well separated from neighbouring defects.

We present theoretical images of 30° dislocations in Fig. 3. We can observe some images of dislocations similar to those in Fig. 3a in the upper part of Fig. 2a.

The agreement of theoretical and experimental images was not quite satisfactory. The simulated images reproduce relatively well the Pendellösung fringes close to the incident beam apart from some problems coming from the saturation of the presently used grey scale in the most dark regions. It may cause that some details

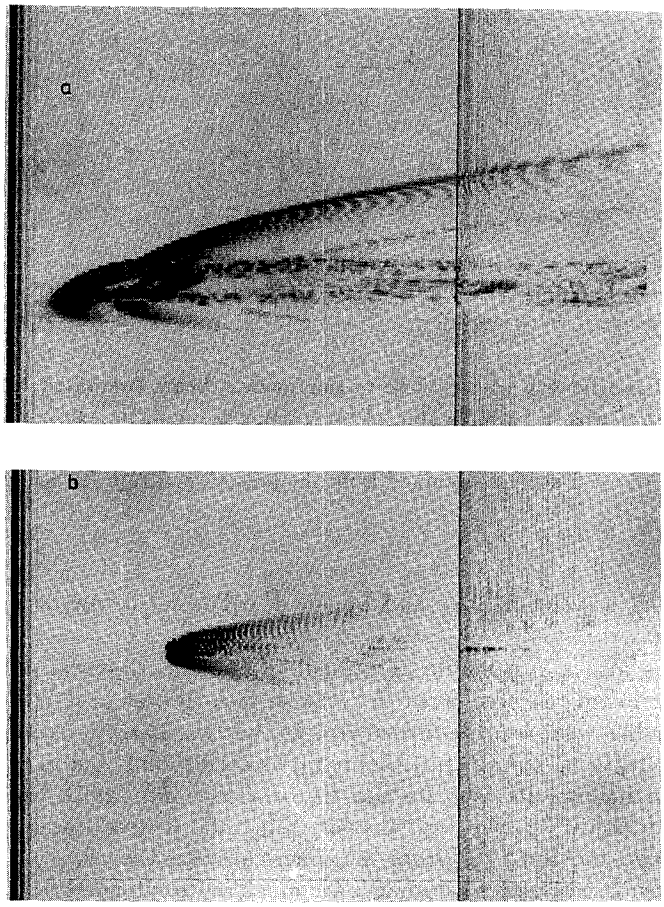

Fig. 3. Theoretical image of 30° dislocation, inclined at 24° to the surface; the dislocation direction is pointing down into the right upper quarter (a). Theoretical image of a 30° dislocation inclined in the vertical plane 35.4° to the surface; the dislocation is located vertically pointing down into the upper part while the fringe system are horizontal (b).

of the theoretical images are reproduced too dark. Also some fine oscillations are deformed due to the resolution of the printed image.

The simulation of the fringe system may be followed in Fig. 4. The fringes appearing close to the single point of incidence are identical to those obtainable from the analytical formula given by Uragami [1]

$$I(x) = Ax^{-2}|J_1\{[\sqrt{\sin(2\theta_B - \Phi)\sin\phi}/\sin 2\theta_B]\alpha x\}|^2,$$

here x is the distance from the point of excitation, Φ is the inclination of reflecting planes, θ_B is the Bragg angle, J_1 denotes the Bessel function and

$$\alpha = \frac{2\pi}{\lambda}\sqrt{\chi_h \chi_{\bar{h}}},$$

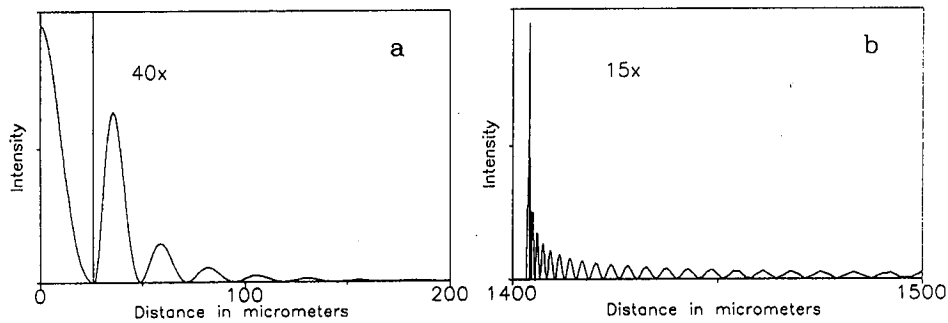

Fig. 4. The Pendellösung fringes close to the incident beam computed by the actually revealed program with a variable step of integration for a single excitation point. The right part of the profile is 40 times enlarged (a). The Pendellösung fringes in the beam reflected from the rear surface obtained from the present program for a single excitation point (b).

where λ is the wavelength, χ_h and $\chi_{\bar{h}}$ are the Fourier component of dielectric susceptibility.

There is also a reasonable agreement of the experimental and theoretical images of the beam reflected from the rear surface. It was practically impossible to resolve further weak and disturbed fringes, but the narrow strip and region of enhanced intensity in experimental topographs correspond well to the theoretical fringes shown in Fig. 4b. The fringes are otherwise similar to those shown by Afanasev and Kohn [3]. The formula describing the fringes was also derived by Saka, Katagawa and Kato [12] from the spherical wave theory.

The considered theoretical images are much more extended and contain more interference fringes that any experimental image of dislocation. The effect is explainable due to several other imperfections, as growth bands, inclusions or other dislocations. In the case of simulated images in Fig. 2a the dislocations outcropped in front of the beam. The incident beam intersected the dislocation line not far from the outcrop. Most of the fringe contrast corresponds to the area of the intersection of the dislocation with the beam and along the dislocation line. The present fringes do not reproduce the dislocation core very strictly. Some contrast appears in the beam reflected from the rear surface.

Both in theoretical and experimental images the deformation field of the dislocation almost does not affect the Pendellösung fringes close to the incident beam.

Taking into account the finite width of the slit in our calculations it produced the images slightly more diffused, but retaining most of the fringe systems. It was found that on the second way of including the slit width we observed more fringe systems at larger slit widths than in the case of the first one. We could observe some fringe systems even for the slit width greater than extinction distance but they should be treated as corresponding to a different diffraction problem. It may be followed in theoretical fringe profiles shown in Fig. 5. In both cases the increase

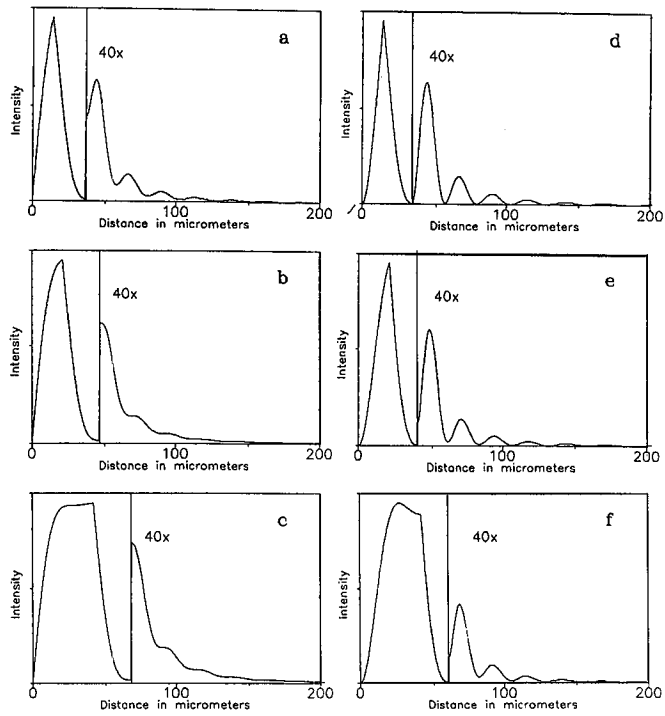

Fig. 5. Comparison of simulated intensity profiles of Bragg-case Pendellösung fringes for different ways of taking into account of the finite width of the slit. The right part of the profile is 40 times enlarged; (a) — adding point source sections at 10 μm slit width; (b) — adding point source sections at 15 μm slit width; (c) — adding point source sections at 30 μm slit width; (d) — adding limited plane waves with a different angle of incidence in the range of 1″ at 10 μm slit width; (e) — adding limited plane waves with a different angle of incidence in the range of 1″ at 15 μm slit width; (f) — adding limited plane waves with a different angle of incidence in the range of 1″ at 30 μm slit width.

of the slit causes lowering of the higher maxima and reducing their resolution. The effect is much more slower at limitation of the beam divergence. Also our other section experiments confirmed that in synchrotron experiments the fringes are visible at much greater slit width than in the case of conventional source section topographs.

The important argument for the proper work of the program and reasonability of computed image is given by the fact that the image practically do not change with the increase or decrease of the integration steps.

5. Conclusions

The Bragg-case section images were obtained in a slab of synthetic diamond using a beam of synchrotron radiation collimated to 1″.

The obtained topographs provided images of various types of defects often containing interference fringes.

The theoretical images of dislocations in Bragg-case section topography was obtained using a variable step integration of Takagi equations. Due to some imperfections of diamond the experimental images were much less extended than the theoretical and contained less interference fringes.

It was found from the present calculation that the additional beam collimation causes better visibility of some fringes at the large slit width.

References

[1] T. Uragami, *J. Phys. Soc. Jpn.* **27**, 147 (1969).

[2] A.R. Lang, Mai Zhen-Hong, *Proc. R. Soc. Lond A* **368**, 313 (1979).

[3] A.M. Afanasev, V.G. Kohn, *Acta Crystallogr. A* **27**, 421 (1971).

[4] E. Zielińska-Rohozińska, *Phys. Status Solidi A* **59**, 317 (1980).

[5] J. Bąk-Misiuk, J. Gronkowski, J. Härtwig, W. Wierzchowski, *Phys. Status Solidi A* **99**, 345 (1987).

[6] P.V. Petrashen, *Fiz. Tverd. Tela* **18**, 3729 (1976).

[7] Y. Epelboin, *Acta Crystallogr. A* **37**, 112 (1981).

[8] W. Wierzchowski, M. Moore, T. Makepeace, A. Yacoot, *J. Cryst. Growth* **114**, 209 (1991).

[9] T. Bedyńska, *Phys. Status Solidi A* **18**, 147 (1973).

[10] Y. Epelboin, M. Gandais, C. Willaime, *Phys. Status Solidi A* **44**, 651 (1977).

[11] S. Shaibani, P. Hazzledine, *Philos. Mag. A* **44**, 657 (1981).

[12] T. Saka, T. Katagawa, N. Kato, *Acta Crystallogr. A* **29**, 192 (1973).